Equation of state in finite-temperature QCD with two flavors of improved Wilson quarks

Equation of state in finite-temperature QCD with two flavors of improved Wilson quarks

A. Ali Khan,[1] S. Aoki,[2] R. Burkhalter,[1,2] S. Ejiri,[1] M. Fukugita,[3] S. Hashimoto,[4] N. Ishizuka,[1,2] Y. Iwasaki,[1,2] K. Kanaya,[2] T. Kaneko,[4] Y. Kuramashi,[4] T. Manke,[1,*] K.-I. Nagai,[1] M. Okamoto,[2] M. Okawa,[4] H. P. Shanahan,[1,†] Y. Taniguchi,[2] A. Ukawa,[1,2] and T. Yoshié[1,2]

(CP-PACS Collaboration)

[1]*Center for Computational Physics, University of Tsukuba, Tsukuba, Ibaraki 305-8577, Japan*
[2]*Institute of Physics, University of Tsukuba, Tsukuba, Ibaraki 305-8571, Japan*
[3]*Institute for Cosmic Ray Research, University of Tokyo, Kashiwa 277-8582, Japan*
[4]*High Energy Accelerator Research Organization (KEK), Tsukuba, Ibaraki 305-0801, Japan*
(Received 23 March 2001; published 10 September 2001)

We present the results of a first study of the equation of state in finite-temperature QCD with two flavors of Wilson-type quarks. The simulations are made on lattices with a temporal size $N_t = 4$ and 6, using a renormalization-group-improved action for the gluon sector and a mean-field-improved clover action for the quark sector. The lines of constant physics corresponding to fixed values of the ratio m_{PS}/m_V of the pseudoscalar to vector meson masses at zero temperature are determined, and the beta functions which describe the renormalization-group flow along these lines are calculated. Using these results, the energy density and the pressure are calculated as functions of temperature along the lines of constant physics in the range $m_{PS}/m_V = 0.65-0.95$. The quark mass dependence in the equation of state is found to be small for $m_{PS}/m_V \lesssim 0.8$. A comparison of the results for $N_t = 4$ and $N_t = 6$ lattices shows a significant scaling violation present in the $N_t = 4$ results. At high temperatures the results for $N_t = 6$ are quite close to the continuum Stefan-Boltzmann limit, suggesting the possibility of a precise continuum extrapolation of thermodynamic quantities from simulations at $N_t \gtrsim 6$.

I. INTRODUCTION

During the last decade, much effort has been devoted to experimentally detecting the quark-gluon plasma state in high energy heavy-ion collisions. In order to extract an unambiguous signal of quark-gluon plasma production from heavy-ion collision experiments, a theoretical understanding of the nature of the finite-temperature chiral phase transition and the thermodynamic properties of quark-gluon plasma is indispensable. In particular, the equation of state (EOS) belongs to the most basic category of information needed in phenomenological investigations of heavy-ion collisions.

Extensive numerical studies have been pursued in lattice QCD to derive the equation of state from first principles [1]. Within the quenched approximation, in which effects of dynamical quark-pair creation and annihilation are neglected, precise results have been established. Continuum extrapolations of the lattice results have been made with various lattice actions, finding a good agreement within errors of a few percent [2–4]. For the pressure, a detailed comparison of the results from the integral method and the derivative method have also been made [5–7]. The problem of a nonzero pressure gap at the transition point with the derivative method has been solved by a nonperturbative calculation of anisotropy coefficients [6].

The next step toward a realistic quark-gluon plasma simulation is to include dynamical quarks, which clearly play a significant role in the real world through chiral symmetry. Until recently, the EOS with dynamical quarks has been computed only with the Kogut-Susskind (staggered) quark action or its improved form [8–10]. Strictly speaking, the staggered quark action only allows the number of flavors to be a multiple of four, and providing a mass difference within the fourfold multiplet is not straightforward. It has also been found that the critical scaling for two-flavor QCD extracted with this formalism [11–14] does not agree with the theoretically expected $O(4)$ values. These features of the Kogut-Susskind quark action make it imperative that the quark-gluon plasma properties be explored with alternative quark actions. In this article we present results on the equation of state obtained with the Wilson quark action in an improved form.

The study of finite temperature QCD with Wilson-type quark action has been difficult for two reasons. First, explicit chiral symmetry breaking complicates the phase diagram analysis [15–17], which is basic for obtaining the equation of state. In this connection, an important role played by the parity-flavor broken phase [18] has been realized, and the phase structure for finite temporal lattice sizes has been understood [19–21].

Another difficulty has been that, when the standard plaquette gauge action and the standard Wilson quark action are adopted, the system exhibits severe lattice artifacts on coarse lattices with a temporal lattice size $N_t = 4$ and 6. For example, the finite-temperature transition strengthens at intermediate quark masses to a first-order transition for N_t

*Present address: Department of Physics, Columbia University, 538 W 120th St., New York, NY 10027.

†Present address: Department of Biochemistry and Molecular Biology, University College London, London, England, United Kingdom.

=6 [16,17], while it should weaken as quarks become heavier. In this regard, it has been shown that an improvement of the gauge action is effective in reducing the lattice artifacts in finite temperature QCD. Furthermore, the critical scaling around the two-flavor chiral transition obtained for a renormalization-group (RG) improved gauge action is consistent with the expected $O(4)$ universality class at $N_t=4$ [22].

These advances indicate that thermodynamic studies with Wilson-type quark actions are feasible if improved actions are employed. We have thus attempted a first calculation of EOS in QCD with two flavors of dynamical quarks, using a RG improved gauge action [23] coupled with a clover-improved Wilson quark action [24]. This combination of actions is motivated from our previous comparative study [25], where we found lattice discretization errors to be small with this action combination in both gluonic and hadronic observables at zero temperature.

The phase structure and the critical temperature for this action combination were studied in Ref. [26], employing an $N_t=4$ lattice. In this paper, we extend the study to an $N_t=6$ lattice. We then calculate the pressure and energy density for $N_t=4$ and 6, employing the integral method [27]. We obtain the EOS as a function of temperature for each fixed value of the renormalized quark mass, i.e., on each line of constant physics. We identify these lines by the ratio of pseudoscalar and vector meson masses, m_{PS}/m_V, at zero temperature. Our results cover EOS's over the range $m_{PS}/m_V =0.65-0.95$.

The organization of the paper is as follows. Our lattice action and the simulation parameters are summarized in Sec. II. In Sec. III, we discuss the phase structure of QCD for our improved Wilson quark action at $N_t=4$ and 6. In Sec. IV, the temperature scale and the lines of constant physics are studied. The RG beta functions, required in our calculation of the EOS, are determined in Sec. V. Results for EOS's at $N_t=4$ and 6 are presented in Sec. VI. Conclusions and discussions are given in Sec. VII.

II. ACTION AND SIMULATION PARAMETERS

The gluon [23] and quark [24] actions we employ are defined by

$$S=S_g+S_q, \tag{1}$$

$$S_g=-\beta\left\{\sum_{x,\mu>\nu}c_0W^{1\times1}_{\mu\nu}(x)+\sum_{x,\mu,\nu}c_1W^{1\times2}_{\mu\nu}(x)\right\}, \tag{2}$$

$$S_q=\sum_{f=1,2}\sum_{x,y}\bar{q}^f_xD_{x,y}q^f_y. \tag{3}$$

Here $\beta=6/g^2$, $c_1=-0.331$, $c_0=1-8c_1$, and

$$D_{x,y}=\delta_{xy}-K\sum_{\mu}\{(1-\gamma_\mu)U_{x,\mu}\delta_{x+\hat{\mu},y}+(1+\gamma_\mu)$$

$$\times U^\dagger_{y,\mu}\delta_{x,y+\hat{\mu}}\}-\delta_{xy}c_{SW}K\sum_{\mu>\nu}\sigma_{\mu\nu}F_{\mu\nu}, \tag{4}$$

TABLE I. Simulation parameters on a $16^3\times4$ lattice.

β	K	Traj.	Therm.
1.80	0.1300–0.1450	500–2000	200–500
1.85	0.1250–0.1440	500–1900	200–300
1.90	0.1250–0.1425	500–2000	200–400
1.95	0.1200–0.1410	500–2000	200
2.00	0.1150–0.1390	500–2000	200–300
2.10	0.0900–0.1375	500–1000	200–900
2.20	0.0700–0.1365	500	200

with $F_{\mu\nu}$ the lattice field strength,

$$F_{\mu\nu}=\frac{1}{8i}(f_{\mu\nu}-f^\dagger_{\mu\nu}), \tag{5}$$

where $f_{\mu\nu}$ is the standard clover-shaped combination of gauge links. For the clover coefficient c_{SW}, we adopt a mean-field value $c_{SW}=P^{-3/4}$ substituting the one-loop result for the plaquette $P=1-0.8412\beta^{-1}$ [23], which agrees within 8% with the values measured in our runs [28]. We also note that the one-loop result $c_{SW}=1+0.678/\beta+\cdots$ [29] is close to our choice $c_{SW}=1+0.631/\beta+\cdots$.

Our two-flavor simulation employs the standard hybrid Monte Carlo (HMC) algorithm. Details of the algorithm implementation are the same as in Refs. [25,26,28]. The length of one trajectory is unity, and the molecular dynamics time step is chosen to yield an acceptance rate greater than about 80%. The inversion of quark matrix is made with the BICGSTAB method. We measure the Polyakov loop and its susceptibility at every trajectory. Jackknife errors of these expectation values are estimated with a bin size of 20–50 trajectories. Hadron propagators are measured at every five trajectories using point and exponentially smeared quark sources.

In Ref. [26], we studied the phase structure for our action combination on $16^3\times4$ lattices with a temporal lattice size $N_t=4$. The simulation parameters are summarized in Table I. The values of the hopping parameter K cover the range $m_{PS}/m_V\approx0.60-0.98$. In these simulations, we have also measured the observables required for the EOS. We have since extended the simulation to an $N_t=6$ lattice. Simulation parameters for $N_t=6$ are compiled in Table II. For the spatial lattice size, we choose $N_s=16$ both for $N_t=4$ and 6. This enables us to commonly apply results obtained on a 16^4 lattice to carry out zero-temperature subtraction in the calculations of the EOS, and to determine the lines of constant physics. For various tests, we also perform simulations on $8^3\times4$ lattices as summarized in Appendix A.

Parameters for the zero temperature simulations are compiled in Table III. On the zero temperature lattice 16^4, we determine meson masses by a combined fit using both point and smeared sources assuming a double hyperbolic cosine form for the propagator. This procedure is necessitated by the fact that a plateau of effective mass is sometimes not quite clear due to a small temporal size of 16. Results for masses are summarized in Table IV, and plotted in Figs. 1 and 2.

TABLE II. Simulation parameters on a $16^3 \times 6$ lattice.

β	K	Traj.	Therm.
1.95	0.1350–0.1410	1000	200
2.00	0.1300–0.1395	800–1500	200
2.10	0.1200–0.1375	500–1000	200–300
2.20	0.1100–0.1365	500–1000	200–300
2.30	0.1000–0.1360	500–1500	200–250

TABLE III. Simulation parameters on a 16^4 lattice.

β	K	Traj.	Therm.
1.80	0.1300–0.1450	200	200–500
1.85	0.1250–0.1440	200–300	100–300
1.90	0.1250–0.1425	200	200–400
1.95	0.1200–0.1410	200–300	100–400
2.00	0.1150–0.1395	200–300	100–200
2.10	0.0900–0.1375	300	200–550
2.20	0.0700–0.1365	200–300	100–200
2.30	0.1000–0.1360	200	100

In order to check the accuracy of mass results, we compare the values of m_{PS} and m_V with those obtained in our previous high statistic simulations [28]. We find that, when $N_t a$ is smaller than about $6/m_{PS}$ ($K = 0.1365$ at $\beta = 2.2$ and $K = 0.1355$ and 0.1360 at $\beta = 2.3$), several masses are inconsistent with those obtained on a $24^3 \times 48$ lattice. In these cases, the effective mass on the 16^4 lattice shows no clear plateau up to the largest time separation 8, suggesting that the temporal lattice size of 16 is not sufficiently large to remove contamination from excited states. Therefore, we do not use data of m_{PS} and m_V on the 16^4 lattice when $N_t a < 6.0/m_{PS}$. We instead include results from our previous study [28], shown by open symbols in Figs. 1 and 2, in the analyses in the present study.

Since the aspect ratio $N_s/N_t = 16/6 = 2.666\ldots$ for $N_t = 6$ is smaller than $N_s/N_t = 4$ for $N_t = 4$, we also check the influence of the spatial volume on the EOS. In the ideal gas limit of $\beta \to \infty$, analytical calculations as described in Appendix B show a 10% finite size correction for $N_s/N_t = 3$ when $N_t \sim 4–6$ as compared to a 5% effect for $N_s/N_t = 4$. Perturbative estimates are not reliable close to the critical temperature, however. To study the spatial volume effect in this region, we make additional simulations at $N_s/N_t = 2$ on $8^3 \times 4$ lattices, and compare the results with those at $N_s/N_t = 4$ obtained on $16^3 \times 4$ lattices. Details are presented in Appendix A. We find that the pressure at $N_s/N_t = 2$ and 4 are consistent with each other within 1–2 %, except very near the critical temperature. We therefore conclude that finite volume corrections are reasonably controlled for our $N_t = 6$ lattices over the range of temperature we study.

III. PHASE STRUCTURE AND PSEUDOCRITICAL TEMPERATURE

Figure 3 summarizes our results for the phase diagram. The solid line threading through filled circles, denoted $K_c(T=0)$, is the location of the critical line where the pion mass vanishes at zero temperature. This is the line of constant physics for massless quarks. Above the $K_c(T=0)$ line, the parity-flavor symmetry of the Wilson-type quark action is broken spontaneously [18,20]. The pion mass vanishes along the line since, the pion becomes the massless mode of a second-order transition associated with this spontaneous breakdown. At zero temperature, the boundary of the parity-flavor broken phase [the $K_c(T=0)$ line] is expected to form a sharp cusp touching the free massless fermion point $K = 1/8$ at $\beta = \infty$.

For finite temporal sizes N_t corresponding to finite temperatures $T = (a N_t)^{-1}$, the parity-flavor broken phase retracts from the large β limit, forming a cusp [19,20]. The boundary of the parity-flavor broken phase at $N_t = 4$, the $K_c(N_t=4)$ line, is shown by a thin line threading through open circles in Fig. 3.

The dashed line $K_t(N_t=4)$ through open diamonds represents the finite-temperature pseudocritical line for a temporal size $N_t = 4$, which is determined from the Polyakov loop and its susceptibility [26]. The region to the right of K_t (larger β) is the high temperature quark-gluon plasma phase, and that to the left of K_t (smaller β) is the low temperature hadron phase. The crossing point of the $K_c(T=0)$ and $K_t(N_t=4)$ lines is the finite-temperature chiral phase transition point [17]. As one observes in Fig. 3, the chiral transition point is located close to the cusp of the parity-flavor broken phase, with the difference expected to be $O(a)$. This is consistent with the picture that the massless pion, interpreted as the Nambu-Goldstone boson associated with spontaneous chiral symmetry breaking in the continuum limit, appears only in the cold phase.

In Figs. 4 and 5 we present the expectation value of the Polyakov loop and its susceptibility obtained on a $16^3 \times 6$ lattice. We find a clear peak of the Polyakov loop susceptibility. Fitting the peak by a Gaussian form using three or four points around the peak, we determine $K_t(N_t=6)$ at $\beta = 2.0$, 2.1, 2.2, and 2.3, as summarized in Table V. The results are shown in Fig. 3 by filled diamonds denoted $K_t(N_t=6)$.

The pseudocritical temperature T_{pc} in units of the zero-temperature vector meson mass was studied in Ref. [26] for $N_t = 4$. We repeat the study using the $N_t = 6$ data. For this purpose, we interpolate the zero-temperature meson mass data to the $K_t(N_t=6)$ line by

$$(m_{PS}a)^2 = B_{PS}\left(\frac{1}{K} - \frac{1}{K_c}\right) + C_{PS}\left(\frac{1}{K} - \frac{1}{K_c}\right)^2, \qquad (6)$$

$$m_V a = B_V\left(\frac{1}{K} - \frac{1}{K_c}\right) + C_V\left(\frac{1}{K} - \frac{1}{K_c}\right)^2. \qquad (7)$$

The values of m_{PS}/m_V and T_{pc}/m_V at K_t are summarized in Table V.

TABLE IV. Results for $m_{PS}a$, $m_V a$, and m_{PS}/m_V on a zero temperature lattice of size 16^4.

β	K	$m_{PS}a$	$m_V a$	m_{PS}/m_V	β	K	$m_{PS}a$	$m_V a$	m_{PS}/m_V
1.80	0.1300	1.7677(41)	1.9318(47)	0.9150(14)	2.00	0.1325	1.1537(35)	1.3047(47)	0.8843(21)
1.80	0.1350	1.5329(40)	1.7384(49)	0.8818(14)	2.00	0.1350	0.9550(37)	1.1159(49)	0.8559(25)
1.80	0.1375	1.3883(45)	1.6310(62)	0.8512(19)	2.00	0.1375	0.7085(34)	0.9044(45)	0.7834(33)
1.80	0.1400	1.2094(35)	1.4769(51)	0.8189(25)	2.00	0.1385	0.6028(47)	0.8291(54)	0.7271(49)
1.80	0.1425	1.0222(44)	1.3368(78)	0.7646(33)	2.00	0.1390	0.5260(35)	0.7439(55)	0.7070(41)
1.80	0.1440	0.8783(63)	1.2198(76)	0.7200(46)	2.00	0.1395	0.4462(40)	0.7114(65)	0.6272(62)
1.80	0.1450	0.7569(46)	1.1563(88)	0.6546(54)	2.10	0.1100	2.1624(22)	2.2109(22)	0.9781(3)
1.85	0.1250	1.9104(48)	2.0410(52)	0.9360(11)	2.10	0.1150	1.9414(25)	1.9989(31)	0.9712(5)
1.85	0.1300	1.6816(35)	1.8440(43)	0.9120(11)	2.10	0.1200	1.6988(21)	1.7683(24)	0.9607(5)
1.85	0.1350	1.4107(44)	1.6148(52)	0.8736(21)	2.10	0.1250	1.4229(17)	1.5066(19)	0.9444(8)
1.85	0.1375	1.2531(32)	1.4862(46)	0.8431(16)	2.10	0.1300	1.1023(23)	1.2044(30)	0.9152(11)
1.85	0.1400	1.0463(38)	1.3170(70)	0.7945(28)	2.10	0.1325	0.9213(26)	1.0429(37)	0.8834(17)
1.85	0.1425	0.8054(37)	1.1233(67)	0.7169(33)	2.10	0.1340	0.7797(41)	0.9059(46)	0.8606(25)
1.85	0.1440	0.5635(46)	0.9488(71)	0.5939(50)	2.10	0.1350	0.7021(22)	0.8453(30)	0.8307(26)
1.90	0.1250	1.8230(38)	1.9470(51)	0.9363(9)	2.10	0.1365	0.5410(27)	0.7152(42)	0.7564(48)
1.90	0.1300	1.5753(39)	1.7283(48)	0.9115(12)	2.10	0.1375	0.4219(39)	0.6158(51)	0.6851(51)
1.90	0.1325	1.4262(41)	1.5979(46)	0.8926(15)	2.20	0.1100	2.0404(21)	2.0765(22)	0.9826(3)
1.90	0.1350	1.2669(39)	1.4550(52)	0.8707(20)	2.20	0.1200	1.5588(21)	1.6129(24)	0.9665(6)
1.90	0.1375	1.0867(33)	1.3126(52)	0.8279(30)	2.20	0.1225	1.4123(28)	1.4695(31)	0.9611(8)
1.90	0.1400	0.8504(50)	1.1186(76)	0.7602(35)	2.20	0.1250	1.2666(25)	1.3323(29)	0.9507(9)
1.90	0.1425	0.4957(54)	0.8292(96)	0.5977(79)	2.20	0.1275	1.1077(22)	1.1788(26)	0.9397(11)
1.95	0.1200	1.9684(45)	2.0643(47)	0.9536(7)	2.20	0.1300	0.9289(26)	1.0167(38)	0.9137(21)
1.95	0.1250	1.7239(43)	1.8360(53)	0.9390(10)	2.20	0.1325	0.7456(33)	0.8442(34)	0.8831(29)
1.95	0.1275	1.6087(38)	1.7398(51)	0.9247(13)	2.20	0.1350	0.5014(31)	0.6307(55)	0.7950(51)
1.95	0.1300	1.4660(37)	1.6155(43)	0.9075(12)	2.30	0.1100	1.9371(18)	1.9655(20)	0.9855(2)
1.95	0.1325	1.2945(42)	1.4530(58)	0.8909(16)	2.30	0.1150	1.6957(20)	1.7314(22)	0.9794(4)
1.95	0.1350	1.1266(38)	1.3138(40)	0.8575(21)	2.30	0.1175	1.5721(20)	1.6102(23)	0.9763(4)
1.95	0.1375	0.9025(39)	1.1177(46)	0.8075(29)	2.30	0.1200	1.4292(20)	1.4692(23)	0.9728(5)
1.95	0.1390	0.7404(33)	0.9789(52)	0.7563(35)	2.30	0.1225	1.2959(20)	1.3397(19)	0.9673(5)
1.95	0.1400	0.5988(38)	0.8510(69)	0.7037(52)	2.30	0.1250	1.1539(29)	1.2074(29)	0.9556(11)
1.95	0.1410	0.4465(35)	0.7424(93)	0.6015(82)	2.30	0.1275	0.9890(25)	1.0495(28)	0.9424(10)
2.00	0.1150	2.0969(35)	2.1699(37)	0.9664(5)	2.30	0.1300	0.8117(25)	0.8812(30)	0.9211(13)
2.00	0.1200	1.8787(41)	1.9662(47)	0.9555(7)	2.30	0.1325	0.6297(29)	0.7110(47)	0.8857(29)
2.00	0.1250	1.6202(36)	1.7238(44)	0.9399(9)	2.30	0.1340	0.4867(33)	0.5932(40)	0.8205(51)
2.00	0.1275	1.4820(39)	1.5985(48)	0.9271(10)	2.30	0.1350	0.3807(36)	0.5080(53)	0.7493(69)
2.00	0.1300	1.3250(33)	1.4574(46)	0.9092(13)					

Results of T_{pc}/m_V as a function of $(m_{PS}/m_V)^2$ are plotted in Fig. 6 for $N_t=4$ [26] and 6. We find, in the range $m_{PS}/m_V=0.65-0.95$ that we study, values of T_{pc}/m_V at $N_t=4$ and 6 agree within about 10%.

IV. LINES OF CONSTANT PHYSICS

In previous studies of EOS's with staggered-type quark actions, the pressure and energy density are determined as functions of temperature for a fixed value of bare quark mass $m_q^{(0)}a$. While $m_q^{(0)}a$ and N_t are practically easy to set in simulations, the system at different temperatures (or values of β) will have different physical quark masses. This is not useful for phenomenological applications, and we need to evaluate the temperature dependence of thermodynamic ob-

servables for a fixed renormalized quark mass, i.e., on a line of constant physics.

We identify the lines of constant physics in the parameter space (β, K) by the values of m_{PS}/m_V at zero temperature. Deferring details of the interpolation procedure of hadron mass data to Sec. V, we show the lines of constant physics corresponding to the values $m_{PS}/m_V=0.65, 0.70, 0.75, 0.80, 0.85, 0.90, 0.95,$ and 0.975 by solid lines in Fig. 7. In this figure, the bold line with open circles represents the critical line $K_c(T=0)$, corresponding to $m_{PS}/m_V=0$. The bold lines with open diamonds and triangles are the K_t lines for $N_t=4$ and 6.

We also attempt to determine the lines of constant temperature. Here we adopt the pseudocritical temperature T_{pc} on the same line of constant physics as the unit of temperature, where the temperature itself is determined through the
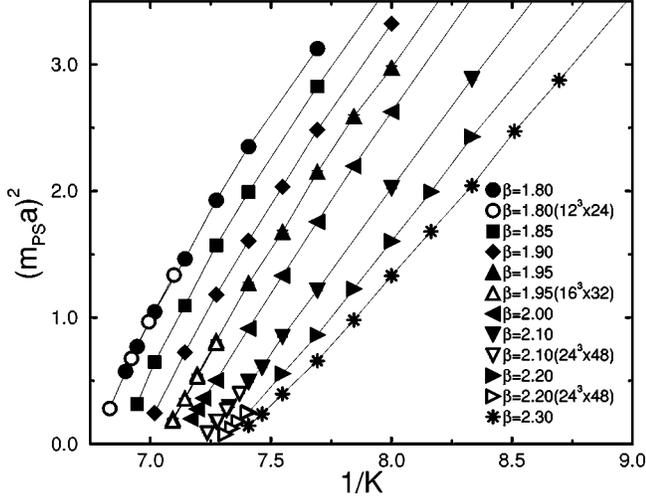
FIG. 1. Pseudoscalar meson mass squared as a function of $1/K$. Filled symbols are obtained on a 16^4 lattice. Open symbols are from Ref. [28].

FIG. 3. Phase diagram and simulation points on $16^3 \times 4$, $16^3 \times 6$, and 16^4 lattices.

zero-temperature vector meson mass $m_V a$ as

$$\frac{T}{m_V}(\beta, K) = \frac{1}{N_t \times m_V a(\beta, K)}. \tag{8}$$

The ratio T_{pc}/m_V for the pseudocritical temperature T_{pc} is obtained by tuning β and K along the K_t line for each N_t. We then interpolate T_{pc}/m_V as a function of $(m_{PS}/m_V)^2$ by a Padé-type ansatz:

$$\frac{T_{pc}}{m_V} = A \frac{1 + B(m_{PS}/m_V)^2}{1 + C(m_{PS}/m_V)^2}. \tag{9}$$

We obtain $A = 0.2253(71)$, $B = -0.933(17)$, and $C = -0.820(39)$ with $\chi^2/N_{df} = 1.61/5$ for $N_t = 4$, and $A = 0.261(19)$, $B = -0.873(35)$, and $C = -0.624(108)$ with $\chi^2/N_{df} = 0.74/1$ for $N_t = 6$. The dashed and dot-dashed lines shown in Fig. 6 are the fit results for $N_t = 4$ and 6.

FIG. 4. Polyakov loop obtained on a $16^3 \times 6$ lattice.

FIG. 5. Polyakov loop susceptibility obtained on a $16^3 \times 6$ lattice.

FIG. 2. Same as in Fig. 1, but for vector meson mass.
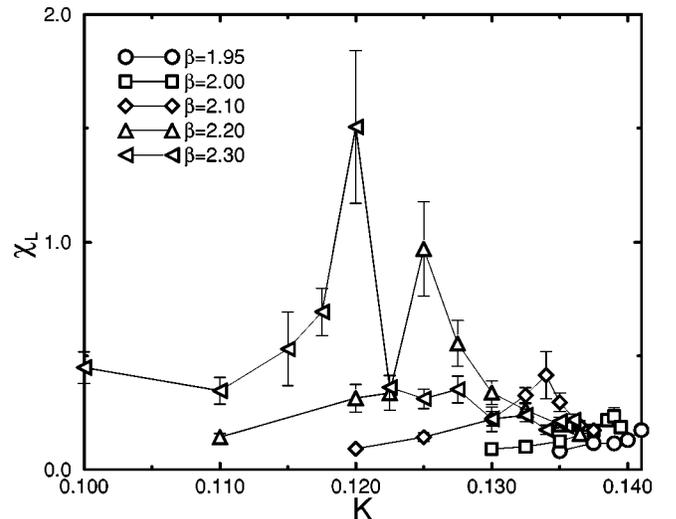
TABLE V. Finite temperature transition and crossover point K_t for $N_t=4$ and 6. Results for $m_{PS}(T=0)/m_V(T=0)$ and $T_{pc}/m_V(T=0)$, interpolated to the K_t point, are also listed.

β	$K_t(N_t=4)$	m_{PS}/m_V	T_{pc}/m_V	$K_t(N_t=6)$	m_{PS}/m_V	T_{pc}/m_V
1.600	0.1543(10)	0.346(153)	0.217(11)			
1.650	0.1533(10)					
1.700	0.1510(10)	0.396(170)	0.234(17)			
1.800	0.1445(14)	0.690(92)	0.211(15)			
1.850	0.14019(18)	0.7905(60)	0.1917(20)			
1.900	0.13621(15)	0.8525(39)	0.1801(12)			
1.925	0.13417(23)					
1.950	0.13040(97)	0.9051(64)	0.1572(62)			
2.000	0.12371(73)	0.9450(36)	0.1398(29)	0.13861(21)	0.725(16)	0.2086(53)
2.100	0.10921(43)	0.9790(13)	0.1114(09)	0.13365(40)	0.8635(78)	0.1753(58)
2.200				0.12539(25)	0.9481(19)	0.1275(15)
2.300				0.11963(15)	0.9724(12)	0.11145(62)

Ansatz (9) does not incorporate the O(4) scaling behavior $T_{pc}(m_{PS})=T_{pc}(0)+cm_{PS}^{2/\beta\delta}$ with $1/\beta\delta=0.54$ expected close to the chiral limit or the constraint $T_{pc}=0$ in the heavy quark limit $m_{PS}/m_V=1$. Fits satisfying these constraints may be attempted, e.g., by replacing $(m_{PS}/m_V)^2$ with $(m_{PS}/m_V)^{2/\beta\delta}$ and giving an additional factor $[1-(m_{PS}/m_V)^2]$. They yield curves which are close to that of Eq. (9) but agree less well with data. Since we employ such fits for the purpose of interpolating the data for T_{pc}/m_V over the quark mass range $m_{PS}/m_V \simeq 0.65-0.95$ of our study, we choose to adopt Eq. (9) in the following analyses.

For $N_t=6$, since the data for T_{pc}/m_V cover only the range $m_{PS}/m_V=0.725-0.972$, we have to extrapolate the fit result down to $m_{PS}/m_V=0.65$. We check the effect of extrapolation by performing a fit of $N_t=4$ data using only the points in the range $m_{PS}/m_V=0.725-0.972$. We find that the difference between this fit and our full fit is less than 1% for $m_{PS}/m_V=0.65-0.7$.

Finally, we normalize the temperature T/m_V by the pseu-

docritical temperature T_{pc}/m_V on the same line of constant physics. Results of the procedure above for the lines of constant temperature are shown by dashed lines in Fig. 7 for $T/T_{pc}=1.0, 1.2, 1.4, 1.6, 1.8,$ and 2.0, where $K_t(N_t=4)$ is used to set T_{pc}. We observe that the K_t line for $N_t=6$ is slightly discrepant from the $T/T_{pc}=1.5$ line; this deviation represents a scaling violation in T_{pc}/m_V.

V. BETA FUNCTIONS

The renormalization group flow along the lines of constant physics is described by the beta functions. Their precise values are required in a calculation of the energy density ϵ/T^4 discussed in Sec. VI. In this section, we study the beta functions

$$a\frac{\partial\beta}{\partial a}\bigg|_{m_{PS}/m_V}, \quad a\frac{\partial K}{\partial a}\bigg|_{m_{PS}/m_V} \quad (10)$$
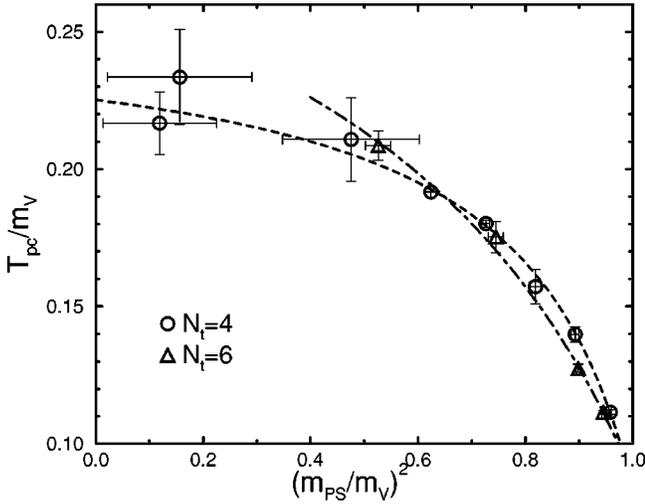

FIG. 6. Pseudocritical temperature in units of the vector meson mass as a function of $(m_{PS}/m_V)^2$. Dashed lines are interpolations, separately, for $N_t=4$ and 6 data.
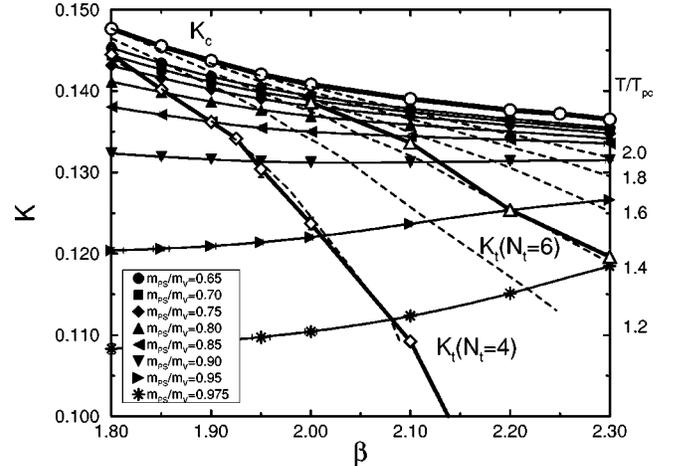

FIG. 7. Lines of constant physics and constant temperature. Solid lines are m_{PS}/m_V constant lines, and dashed lines are T/T_{pc} constant lines for $N_t=4$. The values of T/T_{pc} for the dashed lines are given on the right edge of the figure.

for fixed values of m_{PS}/m_V, using results for $m_{PS}a$ and $m_V a$ at zero temperature.

Since m_V is a physical quantity which we can take as independent of the lattice spacing a, the derivatives $a\partial\beta/\partial a$ and $a\partial K/\partial a$ with fixed m_{PS}/m_V can be replaced by $m_V a\partial\beta/\partial(m_V a)$ and $m_V a\partial K/\partial(m_V a)$. Naively, these quantities may be determined in the following way. First, one fits the values of $m_{PS}a$ and $m_V a$ measured at each (β,K) by a suitable fit function, and differentiates the function in terms of β and K. The derivatives $\partial\beta/\partial(m_V a)$ and $\partial K/\partial(m_V a)$ can be calculated by solving

$$\begin{pmatrix} \dfrac{\partial\beta}{\partial(m_V a)} & \dfrac{\partial K}{\partial(m_V a)} \\[2ex] \dfrac{\partial\beta}{\partial(m_{PS}/m_V)} & \dfrac{\partial K}{\partial(m_{PS}/m_V)} \end{pmatrix}$$
$$= \begin{pmatrix} \dfrac{\partial(m_V a)}{\partial\beta} & \dfrac{\partial(m_{PS}/m_V)}{\partial\beta} \\[2ex] \dfrac{\partial(m_V a)}{\partial K} & \dfrac{\partial(m_{PS}/m_V)}{\partial K} \end{pmatrix}^{-1}. \qquad (11)$$

In practice, however, we find that there exists a region where the matrix on the right hand side becomes almost singular, so that the inverse cannot be solved reliably. In particular, when quarks are heavy, because m_{PS}/m_V is always close to 1, its derivatives in terms of β and K cannot be determined precisely.

This leads us to adopt the following alternative method. We determine $m_V a(\partial\beta/\partial m_V a)$ and $m_V a(\partial K/\partial m_V a)$ directly from the inverse functions $\beta(m_V a, m_{PS}/m_V)$ and $K(m_V a, m_{PS}/m_V)$. In Fig. 8, we plot results for $(m_V a, m_{PS}/m_V)$ at zero temperature. To determine $a\partial\beta/\partial a$ and $a(\partial K/\partial a)$ at a point, say, $[(m_V a)_0, (m_{PS}/m_V)_0]$, we fit data for (β,K), i.e., the values specifying the simulation points, by a power function expanded in terms of $[\Delta(m_V a),\Delta(m_{PS}/m_V)]=[m_V a-(m_V a)_0,(m_{PS}/m_V)-(m_{PS}/m_V)_0]$. We employ the following general fit ansatz up to the third power:

$$\beta = c_{\beta 0} + c_{\beta 1}\{\Delta m_V a\} + c_{\beta 2}\{\Delta m_V a\}^2 + c_{\beta 3}\{\Delta m_V a\}^3$$
$$+ c_{\beta 4}\{\Delta(m_{PS}/m_V)\} + c_{\beta 5}\{\Delta(m_{PS}/m_V)\}\{\Delta m_V a\}$$
$$+ c_{\beta 6}\{\Delta(m_{PS}/m_V)\}\{\Delta m_V a\}^2 + c_{\beta 7}\{\Delta(m_{PS}/m_V)\}^2$$
$$+ c_{\beta 8}\{\Delta(m_{PS}/m_V)\}^2\{m_V a-(m_V a)_0\}$$
$$+ c_{\beta 9}\{\Delta(m_{PS}/m_V)\}^3, \qquad (12)$$

$$K = c_{K0} + c_{K1}\{\Delta m_V a\} + c_{K2}\{\Delta m_V a\}^2 + c_{K3}\{\Delta m_V a\}^3$$
$$+ c_{K4}\{\Delta(m_{PS}/m_V)\} + c_{K5}\{\Delta(m_{PS}/m_V)\}\{\Delta m_{PS}a\}$$
$$+ c_{K6}\{\Delta(m_{PS}/m_V)\}\{\Delta m_V a\}^2 + c_{K7}\{\Delta(m_{PS}/m_V)\}^2$$
$$+ c_{K8}\{\Delta(m_{PS}/m_V)\}^2\{\Delta m_V a\} + c_{K9}\{\Delta(m_{PS}/m_V)\}^3. \qquad (13)$$
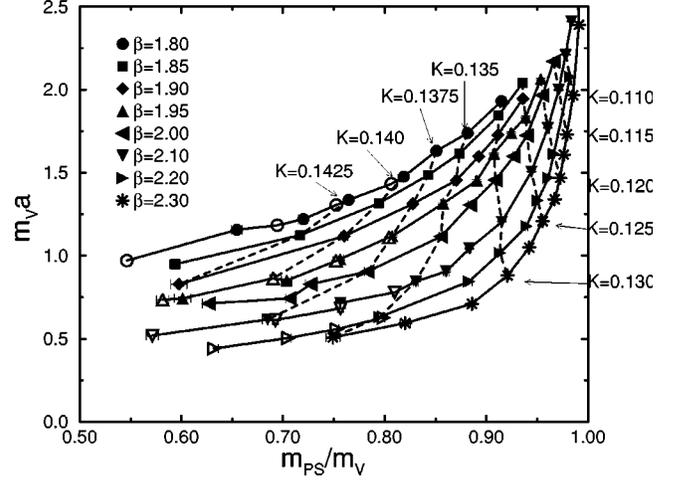

FIG. 8. m_{PS}/m_V vs $m_V a$ obtained on $T=0$ lattices. Solid lines are β constant lines, and dashed lines are K constant lines. The meanings of the symbols are the same as in Fig. 1.

The fit range is determined for each $((m_V a)_0, (m_{PS}/m_V)_0)$ separately: The fit range in m_{PS}/m_V is fixed such that χ^2/N_{df} is minimized, under the condition that the number of fitted data is larger than 30 to avoid artifacts from statistical fluctuations. For the fit range in $m_V a$, we include all data except for the points $m_V a < 2.3$ or $K \geq 0.11$, which are far from the region we study.

From the fit results, we calculate the beta functions by differentiating β and K in terms of $m_V a$, with m_{PS}/m_V fixed:

$$m_V a\frac{\partial\beta}{\partial(m_V a)} = m_V a c_{\beta 1}, \qquad (14)$$

$$m_V a\frac{\partial K}{\partial(m_V a)} = m_V a c_{K1}. \qquad (15)$$

The results are plotted in Figs. 9 and 10. In Fig. 9, the one-loop perturbative value of $m_V a[\partial\beta/\partial(m_V a)]$ for a massless quark is shown by a solid line near the right edge of the plot. Our results appear to approach this value gradually in the large β limit. We also see that $m_V a[\partial K/\partial(m_V a)]$ for small m_{PS}/m_V approaches zero at large β, as we expect from the fact that $K_c \rightarrow 1/8$ as $\beta\rightarrow\infty$. Another application of fits (12) and (13) is the determination of the lines of constant physics and the temperature measured by the vector meson mass, $T/m_V = 1/(N_t m_V a)$, discussed in Sec. IV.

VI. EQUATION OF STATE

The energy density and pressure are defined by

$$\epsilon = -\frac{1}{V}\frac{\partial\ln Z}{\partial T^{-1}}, \quad p = T\frac{\partial\ln Z}{\partial V}, \qquad (16)$$

where Z, T, and V are the partition function, temperature, and spatial volume, respectively. We calculate these quantities as a function of temperature along the lines of constant physics obtained in Sec. IV.
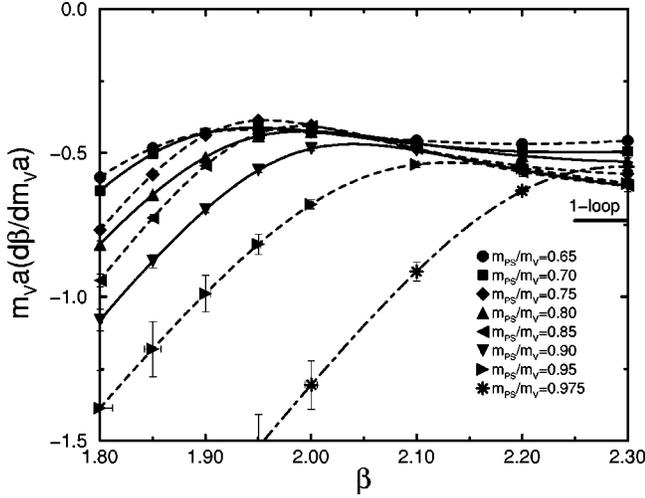
FIG. 9. $m_V a[\partial\beta/\partial(m_V a)]$ on m_{PS}/m_V constant lines. The one-loop result from perturbation theory at $m_q=0$ is also shown.

FIG. 11. Derivative of the pressure with respect to K as a function of K on a $16^3\times4$ lattice.

A. Integral method in full QCD

We compute the pressure by the integral method [27]. This method is based on the formula $p=-f$, with $f=(-T/V)\ln Z$ the free energy density, valid for large homogeneous systems. The pressure is then given by

$$\frac{p}{T^4}=-\frac{f}{T^4}=-N_t^4\int^{(\beta,K)}\mathrm{d}\xi\left\{\left\langle\frac{1}{N_s^3N_t}\frac{\partial S}{\partial\xi}(\beta',K')\right\rangle_{\mathrm{sub}}\right\}\tag{17}$$

where $\mathrm{d}\xi=(\mathrm{d}\beta',\mathrm{d}K')$ is the line element in the (β,K) plane, and $\langle\cdots\rangle_{\mathrm{sub}}$ is the expectation value at finite temperature with the zero-temperature value subtracted. The starting point of the integration path should be chosen in the low temperature phase where $p\approx0$. In actual simulations, for setting the starting point of the integration path, we quadratically extrapolate results for the integrand near the low temperature phase to zero.

For our actions (2) and (3), the derivatives in Eq. (17) are given by
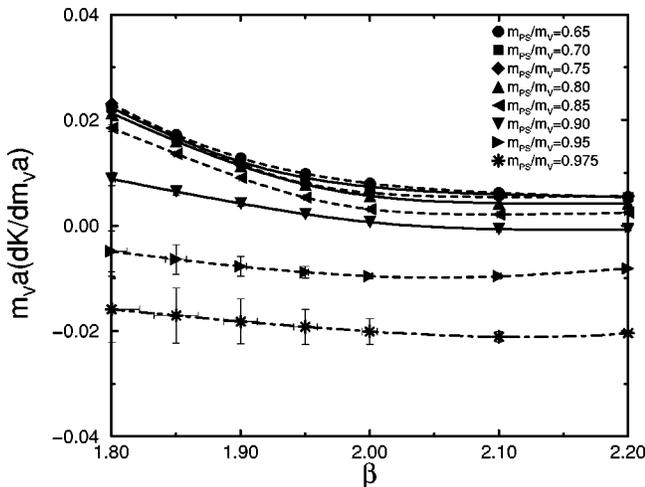

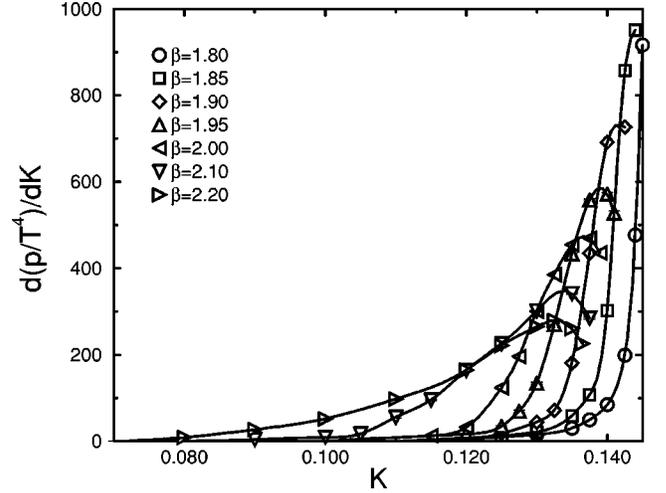FIG. 10. $m_V[a\partial K/\partial(m_V a)]$ on m_{PS}/m_V constant lines.

$$\frac{\partial\ln Z}{\partial\beta}=\left\langle-\frac{\partial S}{\partial\beta}\right\rangle$$

$$=N_s^3N_t\left(\left\langle c_0\sum_{x,\mu>\nu}W_{\mu\nu}^{1\times1}+c_1\sum_{x,\mu,\nu}W_{\mu\nu}^{1\times2}\right\rangle-N_f\frac{\partial c_{SW}}{\partial\beta}K\right.$$

$$\left.\times\left\langle\sum_{x,\mu>\nu}\mathrm{Tr}^{(c,s)}\sigma_{\mu\nu}F_{\mu\nu}(x)D^{-1}(x,x)\right\rangle\right),\tag{18}$$

$$\frac{\partial\ln Z}{\partial K}=\left\langle-\frac{\partial S}{\partial K}\right\rangle$$

$$=N_fN_s^3N_t\left(\left\langle-\sum_{x,\mu}\mathrm{Tr}^{(c,s)}\{(1-\gamma_\mu)U_\mu(x)\right.\right.$$

$$\left.\times D^{-1}(x+\hat\mu,x)+(1+\gamma_\mu)U_\mu^\dagger(x)D^{-1}(x,x+\hat\mu)\}\right\rangle$$

$$\left.-c_{SW}\left\langle\sum_{x,\mu>\nu}\mathrm{Tr}^{(c,s)}\sigma_{\mu\nu}F_{\mu\nu}(x)D^{-1}(x,x)\right\rangle\right),\tag{19}$$

where N_s is the spatial lattice size, and $N_f=2$ denotes the number of flavors. We evaluate the quark contributions $\partial S/\partial\beta$ and $\partial S/\partial K$ using the noisy source method. In order to select the type of noise, we have tested $Z(2)$, $U(1)$, and a complex Gaussian noise with a test run on an $8^3\times4$ lattice. We find that the $U(1)$ and $Z(2)$ noises show a faster convergence than the Gaussian noise in the number of noise ensembles. The difference between the $U(1)$ and $Z(2)$ cases is small, while the $U(1)$ noise shows slightly faster convergence in this test. From this result, we have adopted the $U(1)$ noise in this study.

The integral method was originally developed for a pure gauge system, for which the parameter space is one dimensional. In our case, the parameter space is two dimensional. Therefore, the integration path for the pressure [Eq. (17)] is not unique. We have performed a series of test runs on an $8^3\times4$ lattice, and confirmed the integration path indepen-

TABLE VI. Derivative $-(N_s^3 N_t)^{-1}\langle \partial S/\partial K\rangle$ for $16^3\times 4$, $16^3\times 6$, and 16^4 lattices.

β	K	$-\dfrac{1}{N_s^3 N_t}\left\langle\dfrac{\partial S}{\partial K}\right\rangle$ $16^3\times 4$	$16^3\times 6$	16^4	β	K	$-\dfrac{1}{N_s^3 N_t}\left\langle\dfrac{\partial S}{\partial K}\right\rangle$ $16^3\times 4$	$16^3\times 6$	16^4
1.80	0.1300	−5.3622(47)		−5.4232(59)	2.00	0.1395		4.0484(106)	3.3763(124)
1.80	0.1350	−4.8166(79)		−4.9341(51)	2.10	0.0900	−2.9462(25)		−2.9600(17)
1.80	0.1375	−4.3207(63)		−4.5143(54)	2.10	0.1000	−2.8643(27)		−2.8993(14)
1.80	0.1400	−3.5759(65)		−3.9051(93)	2.10	0.1050	−2.7054(31)		−2.7710(25)
1.80	0.1425	−2.2016(162)		−2.9788(112)	2.10	0.1100	−2.3368(50)		−2.5538(26)
1.80	0.1440	−0.2992(227)		−2.1623(102)	2.10	0.1150	−1.8240(60)		−2.1962(21)
1.80	0.1450	2.1328(221)		−1.4493(102)	2.10	0.1200	−1.0100(60)	−1.6474(34)	−1.6509(29)
1.85	0.1250	−4.7935(43)		−4.8429(33)	2.10	0.1250	0.0614(57)	−0.8130(62)	−0.8219(32)
1.85	0.1300	−4.3596(47)		−4.4437(33)	2.10	0.1300	1.6577(59)	0.5028(66)	0.4794(45)
1.85	0.1350	−3.4384(56)		−3.6678(50)	2.10	0.1325		1.5077(73)	1.3864(71)
1.85	0.1375	−2.6171(80)		−3.0360(71)	2.10	0.1340		2.3734(77)	2.0926(79)
1.85	0.1400	−0.8984(161)		−2.0797(142)	2.10	0.1350	3.9084(51)	2.9291(67)	2.5742(52)
1.85	0.1425	2.6710(146)		−0.6809(104)	2.10	0.1365		3.9064(99)	3.4686(71)
1.85	0.1440	4.5010(140)		0.7871(132)	2.10	0.1375	5.3108(39)	4.6615(65)	4.1983(60)
1.90	0.1250	−3.9170(71)		−3.9860(32)	2.20	0.0700	−2.3029(21)		−2.3022(16)
1.90	0.1300	−3.2151(80)		−3.3875(53)	2.20	0.0800	−2.4132(27)		−2.4469(16)
1.90	0.1325	−2.6335(101)		−2.9136(34)	2.20	0.0900	−2.3649(31)		−2.4697(21)
1.90	0.1350	−1.5613(124)		−2.2669(69)	2.20	0.1000	−2.0985(35)		−2.3012(25)
1.90	0.1375	0.3121(130)		−1.3867(70)	2.20	0.1100	−1.4253(42)	−1.8043(21)	−1.8065(20)
1.90	0.1400	2.6656(93)		−0.0358(137)	2.20	0.1200	−0.0533(45)	−0.6958(26)	−0.6954(24)
1.90	0.1425	4.9308(89)		2.0916(163)	2.20	0.1225		−0.2433(30)	−0.2560(41)
1.95	0.1200	−3.5434(50)		−3.6066(38)	2.20	0.1250	1.1380(43)	0.3244(35)	0.2736(27)
1.95	0.1250	−2.9842(63)		−3.1191(60)	2.20	0.1275		1.0372(42)	0.9297(37)
1.95	0.1275	−2.5015(123)		−2.7719(46)	2.20	0.1300	2.7957(50)	1.9547(36)	1.7599(28)
1.95	0.1300	−1.7833(65)		−2.3076(73)	2.20	0.1325	3.8577(40)	3.0423(41)	2.7646(49)
1.95	0.1325	−0.6182(99)		−1.6726(52)	2.20	0.1350	5.0923(39)	4.4078(41)	4.0746(41)
1.95	0.1350	0.8561(76)	−0.8309(61)	−0.8373(61)	2.20	0.1365	5.8931(36)	5.3480(43)	5.0113(52)
1.95	0.1375	2.4815(64)	0.3734(92)	0.3009(84)	2.30	0.1000		−1.8180(16)	−1.8210(21)
1.95	0.1390		1.3834(87)	1.2217(86)	2.30	0.1100		−1.2098(17)	−1.2178(21)
1.95	0.1400	4.2807(63)	2.3321(134)	2.0463(106)	2.30	0.1150		−0.6777(21)	−0.6944(21)
1.95	0.1410	5.0293(99)	3.6109(165)	2.9673(135)	2.30	0.1175		−0.3082(20)	−0.3570(29)
2.00	0.1150	−3.2222(42)		−3.2710(27)	2.30	0.1200		0.1051(23)	0.0439(28)
2.00	0.1200	−2.7735(49)		−2.8989(40)	2.30	0.1225		0.6267(24)	0.5338(29)
2.00	0.1250	−1.8085(56)		−2.2919(32)	2.30	0.1250		1.2434(23)	1.1185(25)
2.00	0.1275	−1.0607(82)		−1.8253(43)	2.30	0.1275		2.0087(33)	1.8252(21)
2.00	0.1300	−0.0836(73)	−1.2623(54)	−1.2600(49)	2.30	0.1300		2.9362(34)	2.7110(40)
2.00	0.1325	0.9962(91)	−0.5093(40)	−0.5103(75)	2.30	0.1325		4.0641(38)	3.8077(38)
2.00	0.1350	2.2580(69)	0.5282(49)	0.4820(82)	2.30	0.1340		4.8553(29)	4.6173(29)
2.00	0.1375	3.7258(78)	2.0073(86)	1.8917(77)	2.30	0.1350		5.4316(35)	5.1741(50)
2.00	0.1385		2.9849(14)	2.5623(111)	2.30	0.1355		5.7271(42)	5.4944(29)
2.00	0.1390	4.6687(79)	3.4516(133)	2.9676(112)	2.30	0.1360		6.0362(32)	5.8475(45)

dence [30]. Details of the test are presented in Appendix A. We shall present results of a similar test in our production runs below.

From this test we also find that the integration paths in the K direction (constant β) lead to smaller errors for the final values of the pressure than those in the β direction (constant K). Therefore, we choose the integration paths in the K direction starting from the region of small values of K and moving toward the chiral limit. Our simulation points on the $16^3\times 4$ and $16^3\times 6$ lattices are shown by "+" and "×" in Fig. 3.

B. Equation of state for $N_t = 4$

In Fig. 11, we show the results for the pressure derivative

$$\frac{\partial(p/T^4)}{\partial K} = -N_t^4\left\langle\frac{1}{N_s^3 N_t}\frac{\partial S}{\partial K}\right\rangle_{\text{sub}} \qquad (20)$$

obtained on an $N_t = 4$ lattice. Measurements are made with

five noise ensembles at every trajectory. The bin size for the jackknife errors is set to ten trajectories from a study of bin size dependence. Numerical values for the derivative are summarized in Table VI. Interpolating the data by a cubic spline method, we integrate in the K direction to obtain the pressure presented in Fig. 12.

We also compute the derivative in the β direction,

$$\frac{\partial(p/T^4)}{\partial \beta} = -N_t^4 \left\langle \frac{1}{N_s^3 N_t} \frac{\partial S}{\partial \beta} \right\rangle_{\text{sub}}, \quad (21)$$

as shown in Fig. 13 and Table VII. We observe that the results for this derivative are noisier than those for the K derivative in Fig. 11. This is the underlying reason for the fact commented upon in Sec. VI A that the integral paths in the K direction lead to smaller errors in the pressure.

In Fig. 14, we replot the pressure from the K integration as a function of β, and compare it with the slope [Eq. (21)] computed independently from the $\partial S/\partial \beta$ data. The latter data for the slope, shown by short lines, are tangential to the pressure curve, confirming the integration path independence of results for the pressure.

The pressure data shown in Fig. 12 or 14 are not yet quite useful. We wish to compute the pressure on a line of constant physics as a function of temperature normalized by the pseudocritical temperature T_{pc} on the same line of constant physics. The necessary change of parameters from (β, K) to $(m_{\text{PS}}/m_{\text{V}}, T/T_{pc})$ is achieved with the interpolations performed in Secs. IV and V.

The pressure p/T^4 as a function of T/T_{pc} is given in Fig. 15 for $m_{\text{PS}}/m_{\text{V}} = 0.65, 0.7, 0.75, 0.8, 0.85, 0.9$, and 0.95. In this figure, symbols denote the values on the integration path along the K direction at $\beta = 1.80, 1.85, 1.90, 1.95, 2.00, 2.10$, and 2.20, i.e., for each β, the pressure in Fig. 12 at the values of K corresponding to the given values of $m_{\text{PS}}/m_{\text{V}}$. The values of T/T_{pc} at those points are determined from $m_{\text{V}} a$, as discussed in Sec. IV. To interpolate these symbols in the direction of β (i.e., of T/T_{pc}), we use the results for the slopes $\partial S/\partial \beta$ shown in Fig. 14 and adopt a cubic ansatz.

In Fig. 15 we observe that the pressure depends only weakly on the quark mass once the ratio $m_{\text{PS}}/m_{\text{V}}$ falls below ≈ 0.8. In the heavy quark limit $m_{\text{PS}}/m_{\text{V}} = 1$, the pressure should coincide with the pure gauge value on a lattice with the same size, which is denoted by a dashed line [3]. While the pressure decreases for $m_{\text{PS}}/m_{\text{V}} = 0.80-0.95$, the values at $m_{\text{PS}}/m_{\text{V}} = 0.95$ are still large compared to those of the pure gauge system for $N_t = 4$.

In Fig. 15, we also mark the high-temperature Stefan-Boltzmann (SB) values by solid horizontal lines, both for $N_t = 4$ and in the continuum. The lattice value is evaluated from the free energy density in the SB limit, to be in parallel with the integral method adopted in numerical simulations. Some details of this computation are described in Appendix B. We observe that the pressure overshoots the SB value in the continuum limit, and appears to increase gradually toward the SB value for the $N_t = 4$ lattice at high temperatures. Another point to note is that the large SB value on an $N_t = 4$ lattice [3,31] is dominated by the quark contribution.
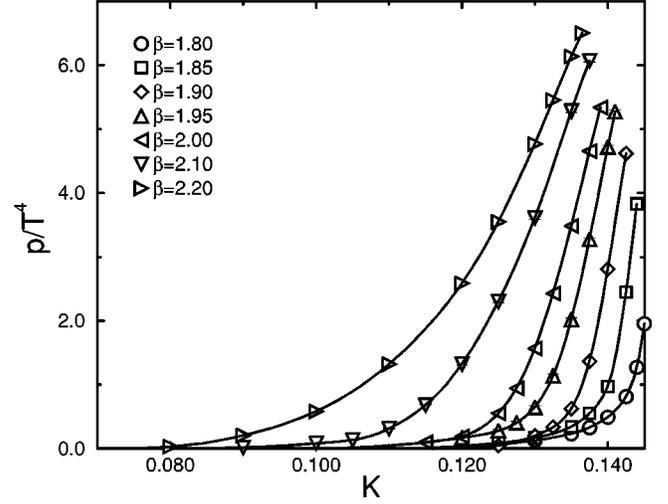

FIG. 12. Pressure as a function of K on a $16^3 \times 4$ lattice.

While the integral method does not allow a separate evaluation of the two contributions, a comparison of the two-flavor result and that of the pure gluon theory [3] (dashed line) shows that the situation should be similar at finite temperatures.

To compute the energy density, we use the following expression for the interaction measure $\epsilon - 3p$:

$$\frac{\epsilon - 3p}{T^4} = N_t^4 \left\langle \frac{1}{N_s^3 N_t} a \frac{\partial S}{\partial a} \right\rangle_{\text{sub}}$$

$$= N_t^4 \left[a \frac{\partial \beta}{\partial a} \left\langle \frac{1}{N_s^3 N_t} \frac{\partial S}{\partial \beta} \right\rangle_{\text{sub}} + a \frac{\partial K}{\partial a} \left\langle \frac{1}{N_s^3 N_t} \frac{\partial S}{\partial K} \right\rangle_{\text{sub}} \right]. \quad (22)$$

Applying the beta functions calculated in Sec. V, we find the results for $(\epsilon - 3p)/T^4$ shown in Fig. 16. The meaning of symbols is the same as in Fig. 15.
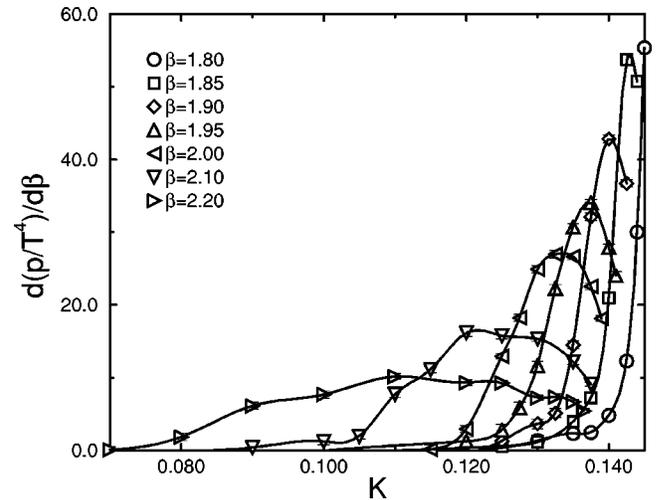

FIG. 13. Derivative of the pressure with respect to β as a function of K on a $16^3 \times 4$ lattice.

TABLE VII. Derivative $-(N_s^3 N_t)^{-1}\langle \partial S/\partial \beta \rangle$ for $16^3 \times 4$, $16^3 \times 6$, and 16^4 lattices.

β	K	$-\dfrac{1}{N_s^3 N_t}\left\langle\dfrac{\partial S}{\partial \beta}\right\rangle$ $16^3\times4$	$16^3\times6$	16^4	β	K	$-\dfrac{1}{N_s^3 N_t}\left\langle\dfrac{\partial S}{\partial \beta}\right\rangle$ $16^3\times4$	$16^3\times6$	16^4
1.80	0.1300	10.0029(19)		9.9976(24)	2.00	0.1395		11.5281(9)	11.5002(12)
1.80	0.1350	10.1115(21)		10.1025(16)	2.10	0.0900	11.3777(16)		11.3762(10)
1.80	0.1375	10.1788(14)		10.1691(14)	2.10	0.1000	11.4407(14)		11.4358(10)
1.80	0.1400	10.2635(11)		10.2447(19)	2.10	0.1050	11.4793(11)		11.4717(11)
1.80	0.1425	10.3846(18)		10.3365(19)	2.10	0.1100	11.5402(12)		11.5100(12)
1.80	0.1440	10.5236(20)		10.4063(15)	2.10	0.1150	11.5992(14)		11.5558(9)
1.80	0.1450	10.6747(17)		10.4585(11)	2.10	0.1200	11.6708(15)	11.6093(13)	11.6077(10)
1.85	0.1250	10.2304(16)		10.2282(10)	2.10	0.1250	11.7271(15)	11.6670(15)	11.6654(10)
1.85	0.1300	10.3234(15)		10.3189(12)	2.10	0.1300	11.7937(11)	11.7355(11)	11.7338(9)
1.85	0.1350	10.4519(12)		10.4365(10)	2.10	0.1325		11.7793(10)	11.7709(13)
1.85	0.1375	10.5354(12)		10.5071(16)	2.10	0.1340		11.8120(8)	11.7991(13)
1.85	0.1400	10.6794(16)		10.5974(23)	2.10	0.1350	11.8604(11)	11.8278(8)	11.8128(10)
1.85	0.1425	10.9123(13)		10.7024(13)	2.10	0.1365		11.8562(12)	11.8402(9)
1.85	0.1440	10.9962(13)		10.7981(15)	2.10	0.1375	11.8958(8)	11.8759(9)	11.8603(8)
1.90	0.1250	10.5626(27)		10.5575(13)	2.20	0.0700	11.7472(13)		11.7468(9)
1.90	0.1300	10.6646(21)		10.6503(16)	2.20	0.0800	11.7854(18)		11.7782(10)
1.90	0.1325	10.7297(23)		10.7098(8)	2.20	0.0900	11.8419(15)		11.8180(10)
1.90	0.1350	10.8326(16)		10.7761(14)	2.20	0.1000	11.8947(14)		11.8647(13)
1.90	0.1375	10.9763(14)		10.8509(16)	2.20	0.1100	11.9626(13)	11.9254(8)	11.9229(10)
1.90	0.1400	11.1143(11)		10.9470(19)	2.20	0.1200	12.0347(12)	11.9996(7)	11.9983(8)
1.90	0.1425	11.2077(11)		11.0643(14)	2.20	0.1225		12.0223(7)	12.0216(8)
1.95	0.1200	10.8016(20)		10.7967(16)	2.20	0.1250	12.0809(11)	12.0477(7)	12.0447(8)
1.95	0.1250	10.8873(17)		10.8763(24)	2.20	0.1275		12.0752(7)	12.0687(7)
1.95	0.1275	10.9443(25)		10.9215(16)	2.20	0.1300	12.1265(11)	12.1065(8)	12.0982(9)
1.95	0.1300	11.0181(11)		10.9724(19)	2.20	0.1325	12.1536(10)	12.1351(10)	12.1249(11)
1.95	0.1325	11.1191(14)		11.0320(13)	2.20	0.1350	12.1805(9)	12.1631(10)	12.1543(7)
1.95	0.1350	11.2183(10)	11.0978(12)	11.0983(14)	2.20	0.1365	12.1936(9)	12.1834(10)	12.1724(7)
1.95	0.1375	11.3012(9)	11.1747(12)	11.1681(15)	2.30	0.1000		12.2137(7)	12.2135(9)
1.95	0.1390		11.2302(11)	11.2194(14)	2.30	0.1100		12.2598(7)	12.2593(9)
1.95	0.1400	11.3700(9)	11.2747(12)	11.2609(14)	2.30	0.1150		12.2893(7)	12.2887(9)
1.95	0.1410	11.3929(15)	11.3272(12)	11.2989(12)	2.30	0.1175		12.3066(6)	12.3021(9)
2.00	0.1150	11.0363(18)		11.0357(13)	2.30	0.1200		12.3234(6)	12.3187(9)
2.00	0.1200	11.1091(12)		11.0977(14)	2.30	0.1225		12.3420(6)	12.3348(8)
2.00	0.1250	11.2205(11)		11.1699(10)	2.30	0.1250		12.3604(7)	12.3550(11)
2.00	0.1275	11.2887(14)		11.2175(12)	2.30	0.1275		12.3812(8)	12.3722(7)
2.00	0.1300	11.3605(14)	11.2629(12)	11.2631(14)	2.30	0.1300		12.4034(9)	12.3947(9)
2.00	0.1325	11.4221(15)	11.3149(8)	11.3168(13)	2.30	0.1325		12.4241(8)	12.4180(10)
2.00	0.1350	11.4778(12)	11.3783(8)	11.3736(12)	2.30	0.1340		12.4368(8)	12.4337(8)
2.00	0.1375	11.5332(13)	11.4481(9)	11.4451(12)	2.30	0.1350		12.4464(8)	12.4401(8)
2.00	0.1385		11.4902(10)	11.4710(13)	2.30	0.1355		12.4497(9)	12.4454(8)
2.00	0.1390	11.5571(13)	11.5063(10)	11.4862(10)	2.30	0.1360		12.4550(7)	12.4509(11)

Combining Figs. 15 and 16 for p/T^4 and $(\epsilon-3p)/T^4$, we obtain the energy density plotted in Fig 17. This quantity also overshoots the SB value in the continuum limit. In contrast to the case of pressure, the energy density in the high temperature phase is quite constant as a function of temperature.

Our results for pressure and energy density allow us to calculate the speed of sound c_s defined by

$$c_s^2 = \frac{\partial p}{\partial \epsilon}. \tag{23}$$

We compute the derivative from a quadratic fit of p as a function of ϵ using three data points along the lines of constant physics. The results for $N_t=4$ are plotted in Fig. 18, where errors are estimated by error propagation from those
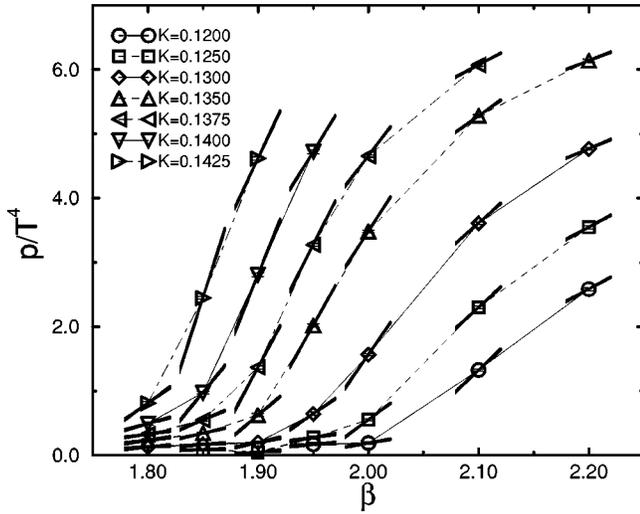
FIG. 14. Pressure as a function of β on a $16^3 \times 4$ lattice. Short lines denote the slope of the pressure for β direction.
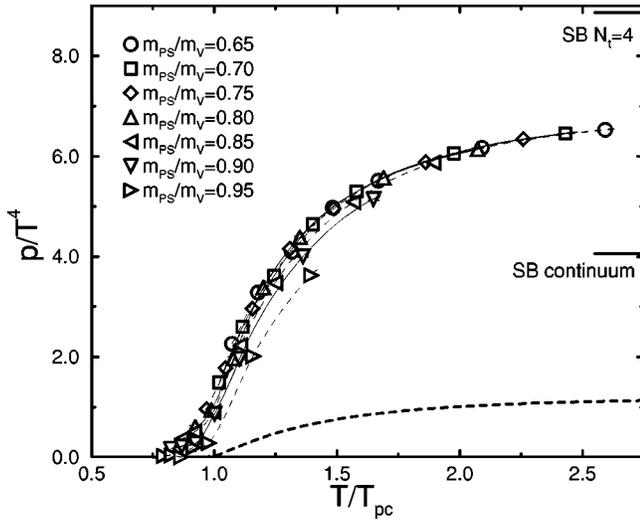

FIG. 15. Pressure on a $16^3 \times 4$ lattice as a function of T/T_{pc}. The dashed curve shows the pressure for pure gauge theory with the RG-improved action on a $16^3 \times 4$ lattice [3].
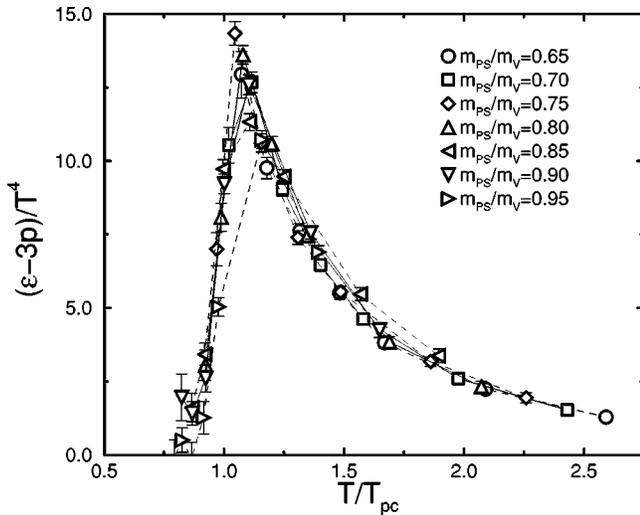

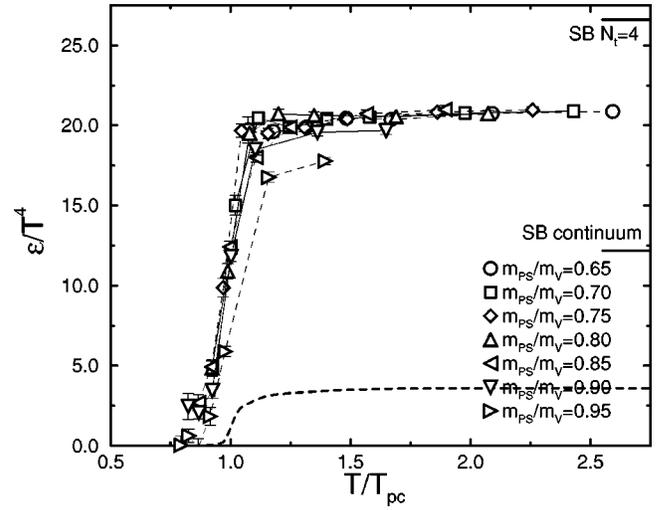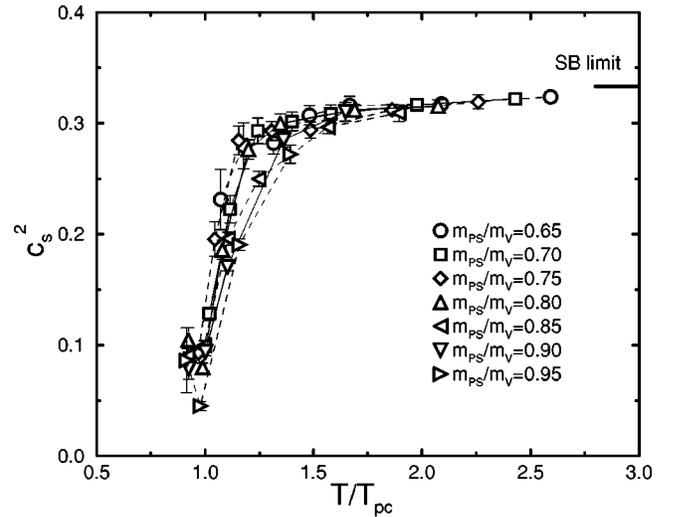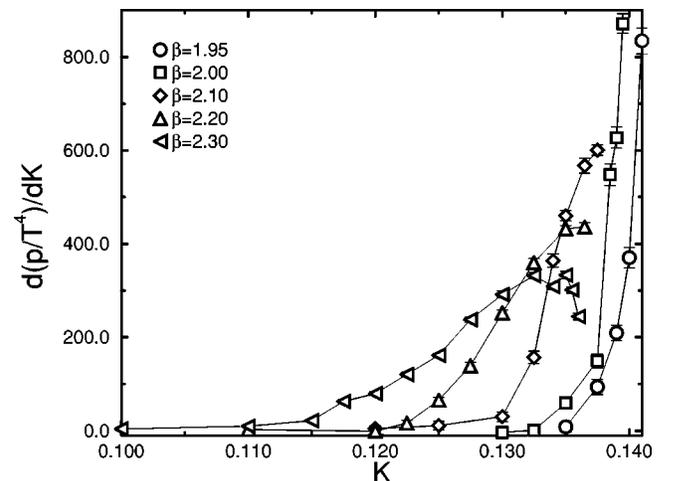FIG. 16. $(\epsilon - 3p)/T^4$ on a $16^3 \times 4$ lattice as a function of T/T_{pc}.

FIG. 17. Energy density on a $16^3 \times 4$ lattice as a function of T/T_{pc}. The dashed curve shows the energy density for pure gauge theory with the RG-improved action on a $16^3 \times 4$ lattice [3].

FIG. 18. Speed of sound squared on a $16^3 \times 4$ lattice as a function of T/T_{pc}.

FIG. 19. Derivative of pressure with respect to K as a function of K on a $16^3 \times 6$ lattice.
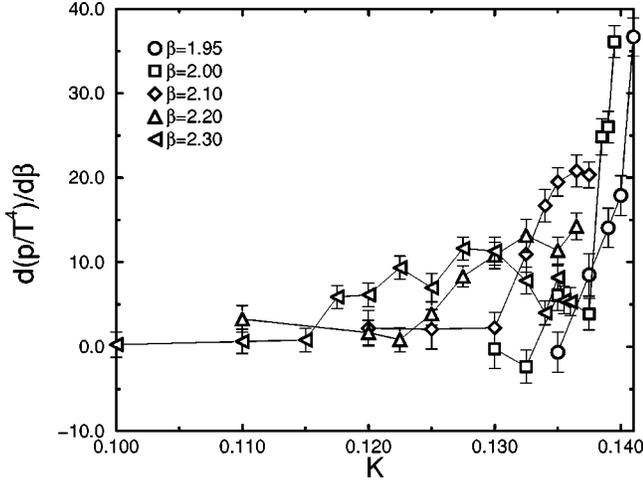
FIG. 20. Derivative of pressure with respect to β as a function of K on a $16^3 \times 6$ lattice.

of p and ϵ. We omit results at small temperatures with $T/T_{ps} < 0.9$, since there the magnitude of ϵ is small in comparison with its error. The speed of sound rapidly increases just above the critical temperature, and almost saturates the SB value when $T/T_{pc} \gtrsim 1.5$.

C. Equation of state for $N_t = 6$

The simulation points for $N_t = 6$ lattices at $\beta = 1.95$, 2.00, 2.10, 2.20, and 2.30 are marked by crosses in Fig. 3. Raw data for the derivatives $\partial(p/T^4)/\partial K$ and $\partial(p/T^4)/\partial \beta$ are shown in Figs. 19 and 20, respectively. Since the statistical errors for $N_t = 6$ results are larger than those for $N_t = 4$, the spline interpolation does not work well for $N_t = 6$. Therefore, we interpolate the pressure derivatives by straight lines. The rest of data analyses parallel those for the case of $N_t = 4$.

The pressures for $N_t = 6$ on the lines of constant physics are plotted in Fig. 21 by open symbols as a function of T/T_{pc}, together with the results for $N_t = 4$ (filled symbols).
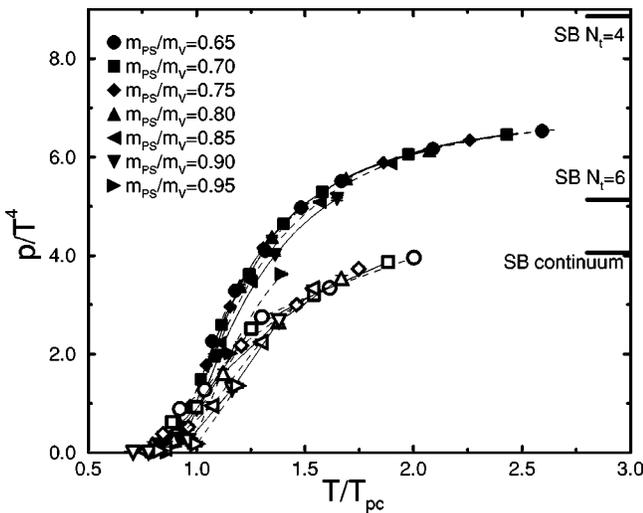

FIG. 21. Pressure on $16^3 \times 4$ (filled symbols) and $16^3 \times 6$ (open symbols) lattices as a function of T/T_{pc}.
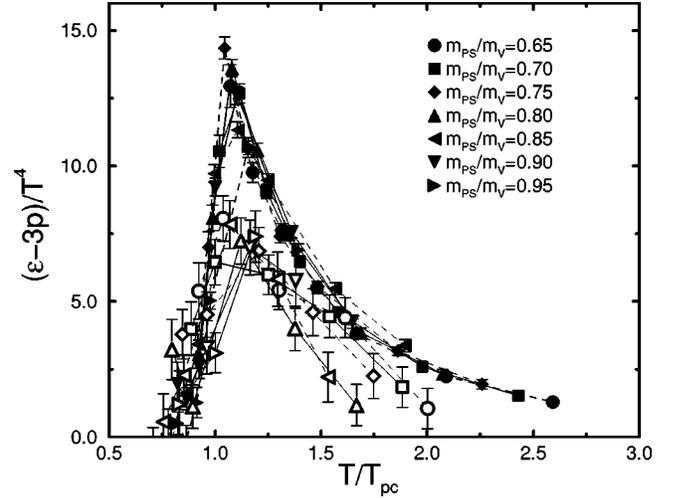

FIG. 22. $(\epsilon - 3p)/T^4$ on $16^3 \times 4$ (filled symbols) and $16^3 \times 6$ (open symbols) lattices as a function of T/T_{pc}.

Figure 22 shows the interaction measure $(\epsilon - 3p)/T^4$ as a function of T/T_{pc}, calculated from results in Figs. 19 and 20 together with the beta functions of Figs. 9 and 10. Combining the results for pressure and interaction measure, we obtain the energy density presented in Fig. 23.

These figures show that both the pressure and energy density decrease as the lattice spacing becomes smaller from $N_t = 4$ to $N_t = 6$, and the values at high temperatures become closer to the continuum SB limit. On the other hand, both at $N_t = 4$ and 6, the energy density is smaller than the SB values for the corresponding N_t, and an approach to the lattice SB value toward high temperatures is not apparent in our data. A similar deviation of the energy density from the SB value at finite N_t was reported in Ref. [3] for the case of the SU(3) pure gauge theory using the RG improved gauge action [Eq. (2)]. Further study is necessary to examine if deviations remain toward the limit of high temperatures.

We also observe for both the pressure and the energy density that the dependence on the quark mass is quite small for
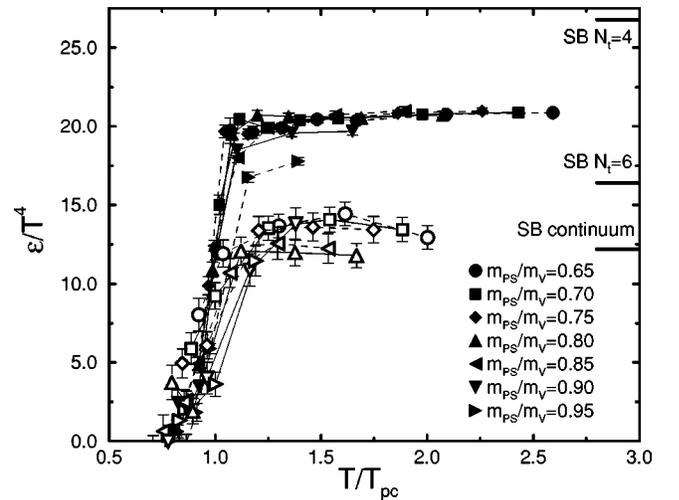

FIG. 23. Energy density on $16^3 \times 4$ (filled symbols) and $16^3 \times 6$ (open symbols) lattices as a function of T/T_{pc}.

$m_{PS}/m_V \approx 0.65-0.8$. A weak quark mass dependence appears only at $m_{PS}/m_V \gtrsim 0.9$ for $N_t=4$ (the errors are still too large to conclude that there is a quark mass dependence for the $N_t=6$ data). This result may not be surprising since hadron mass results in our zero-temperature simulations [28] show that the renormalized quark mass at $\mu=2$ GeV in the modified minimal subtraction ($\overline{\text{MS}}$) scheme at $m_{PS}/m_V \approx 0.65-0.8$ is equal to $m_q^{\overline{\text{MS}}}(\mu=2 \text{ GeV}) \approx 100-200$ MeV, which is similar in magnitude to the critical temperature $T_c \approx 170$ MeV estimated for two-flavor QCD [1]. For comparison, finite mass corrections for free fermion gas only amount to 7% when the temperature equals the fermion mass m_f, and exceed 50% only when $m_f/T \gtrsim 3$.

In a previous study using the standard staggered quark action, it was reported that the energy density ϵ/T^4 for $N_t=4$ overshoot the SB value forming a sharp peak just above T_c, while the results for $N_t=6$ show no peak [8]. With the improved Wilson quark action, we do not observe an overshoot of the energy density both at $N_t=4$ and 6. A similar absence of the peak of energy density was also reported from an improved staggered quark action at $N_t=4$ when a contribution proportional to the bare quark mass is removed [10,32]. We think it likely that the overshoot observed with staggered quark action at $N_t=4$ is a lattice artifact. With the staggered quark action, the energy densities for $m_q/T = 0.075$ and 0.15 at $N_t=6$ are found to be consistent with each other within the errors [8]. This result is similar to our finding of small quark mass dependence in the EOS.

Our present data for $N_t=4$ and 6 show a 50% decrease both in the pressure and energy density, which are too large to attempt a continuum extrapolation. On $N_t=6$ lattices, however, the magnitude and temperature dependence of the two quantities are quite similar between our improved Wilson quark action and the staggered quark action. Together with the fact that the $N_t=6$ results are close to the continuum SB limit at high temperatures, the approximate agreement of EOS's between two different types of actions may be suggesting that the $N_t=6$ results are not far from the continuum limit. This expectation is also supported by the N_t dependence of the SB value on the lattice. The value for $N_t=6$, which is 50% too large compared to the continuum limit, reduces by 30% so that for $N_t=8$ the lattice SB value is within 20% of the continuum limit. Thus we expect that a precise continuum extrapolation will be possible if additional data points at $N_t=8$ are generated, which we leave for future work.

VII. CONCLUSION

We have presented first results for the equation of state in QCD with two flavors of dynamical quarks using a Wilson-type quark action. In order to suppress large lattice artifacts observed with the standard Wilson quark action, we have adopted a clover-improved form of the action and a RG-improved gluon action. Two temporal lattice sizes, $N_t=4$ and 6, are studied to examine the magnitude of finite lattice spacing errors.

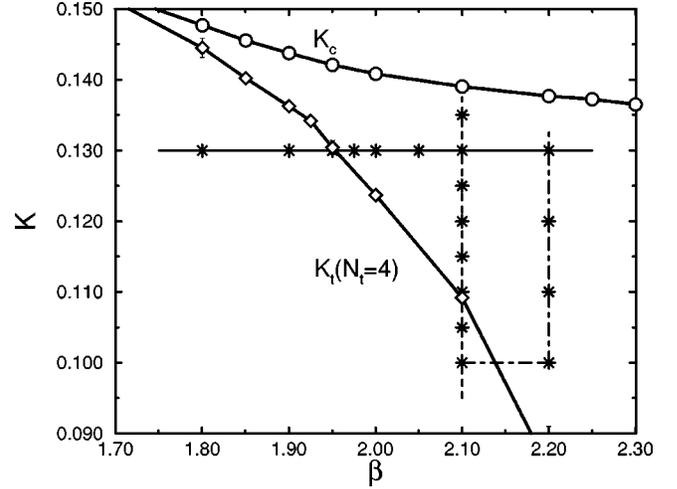We have calculated the energy density and pressure as

FIG. 24. Integration paths for test simulations on an $8^3 \times 4$ lattice. Stars represent the simulation points.

functions of temperature along the lines of constant physics, which are identified through the mass ratio m_{PS}/m_V. As a part of the analysis to work out these lines, we have also computed the beta functions in the parameter space (β, K).

We found that the quark mass dependence of the EOS is small over the range $m_{PS}/m_V \approx 0.65-0.8$. While the physical point $m_{PS}/m_V=0.18$ is still far away, the observed independence on the quark mass suggests that our result for the EOS is close to those at the physical point except in the vicinity of the chiral transition point, where a singular limit according to the O(4) critical exponents is expected.

Our results for the pseudocritical temperature, in units of the vector meson mass T_{pc}/m_V, show an agreement within about 10% between the temporal lattice sizes $N_t=4$ and 6. On the other hand, the pressure and the energy density decrease substantially, showing the presence of large scaling violation in the results for $N_t=4$. An encouraging indication, however, is that results on the $N_t=6$ lattice are close to the continuum Stefan-Boltzmann value at high temperatures. We
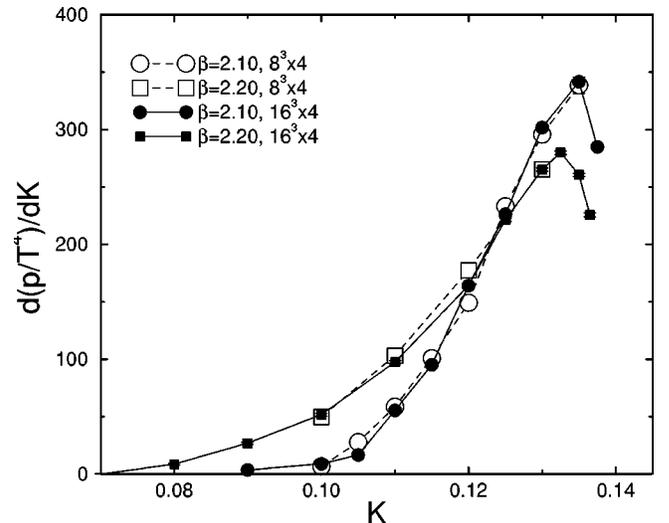

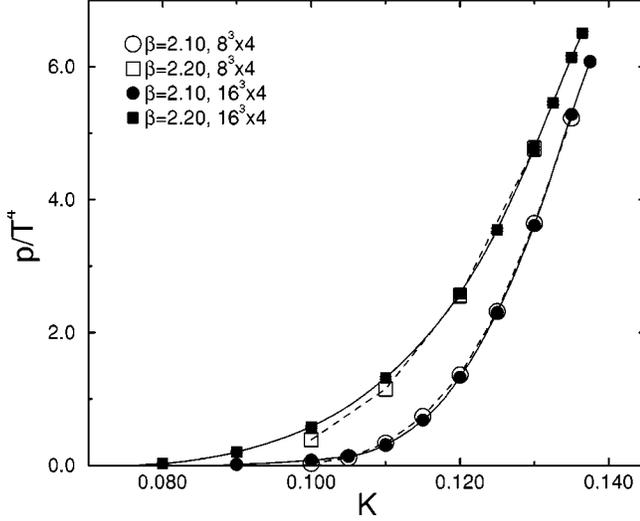FIG. 25. $\partial(p/T^4)/\partial K$ on $8^3 \times 4$ and $16^3 \times 4$ lattices.

FIG. 26. The pressure p/T^4 on $8^3 \times 4$ and $16^3 \times 4$ lattices.

also note that the values and the temperature dependence of the EOS at $N_t = 6$ are quite similar to the previous results from staggered quark action [8]. These may be suggestions of a possibility that precise calculations of the EOS are realized on lattices with temporal sizes N_t not much larger than 6.

APPENDIX A: A TEST OF THE INTEGRAL METHOD IN FULL QCD

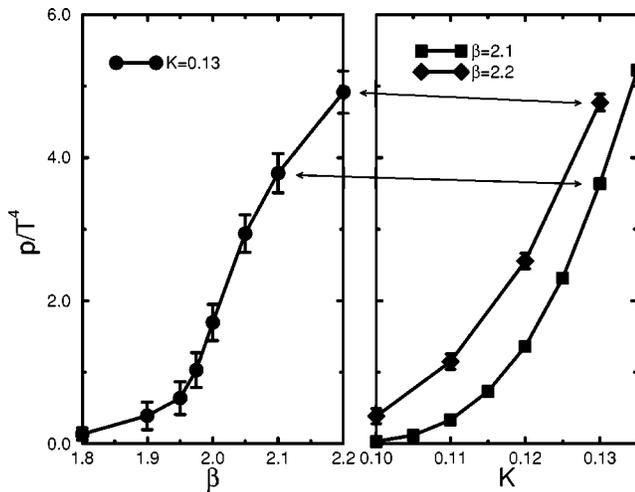We compute the EOS by the integral method [27] described in Sec. VI A. In order to test the method, we perform

FIG. 27. Pressure computed along integration paths at $K = 0.13$ (left) and $\beta = 2.1$ and 2.2 (right) on an $8^3 \times 4$ lattice.

a series of test runs to calculate the pressure on an $8^3 \times 4$ lattice. For subtraction of the zero temperature part, we also measure the same operators on an 8^4 lattice. Simulation points are shown by stars in Fig. 24. We generate 500 HMC trajectories at each point.

We first check the influence of the spatial volume on the EOS. In order to avoid systematic errors from the numerical interpolation and extrapolation needed for numerical integrations, we first compare the values of the integrand $\partial(p/T^4)/\partial K$ for $N_s/N_t = 2$ ($8^3 \times 4$ lattice) with those for $N_s/N_t = 4$ from our main runs on a $16^3 \times 4$ lattice. From Fig. 25, we find that the difference between $N_s/N_t = 2$ and 4 is comparable with statistical fluctuations. Integrating out these values, we obtain Fig. 26. We find that the two results agree well with each other—the slight discrepancy of the $\beta = 2.2$ data at small K seems to be caused by a longer extrapolation to the point $\partial(p/T^4)/\partial K = 0$ for the stating point of the integration.

We then test the integration path independence in the integral method. We study three integration paths in the parameter space (β, K), shown in Fig. 24. At the crossing points, the results for the pressure from different paths should coincide with each other. The results for p/T^4, obtained from these paths, are summarized in Fig. 27. The left figure is obtained by integrating in the β direction at $K = 0.13$, while the right figure is computed from the integration paths in the K direction at $\beta = 2.1$ and 2.2.

We find that p/T^4 at $(\beta, K) = (2.1, 0.13)$ and $(2.2, 0.13)$ in the two figures agree well with each other. This confirms the path independence of the pressure.

We also note that the paths in the K direction lead to much smaller errors in the pressure than the path in the β direction. We therefore adopt paths in the K direction in the production runs discussed in the main text.

APPENDIX B: STEFAN-BOLTZMANN LIMIT OF PRESSURE BY THE INTEGRAL METHOD

In the calculation of pressure discussed in Sec. VI, we employ the integral method, in which the negative of free energy density $-f = (T/V)\ln Z$ is identified with the pressure. In order to compute the Stefan-Boltzmann value to be compared with the pressure from the integral method, we should compute the free energy density in the free gas limit. In this appendix, we describe our calculation of the free energy density for the case of our improved lattice action.

To calculate the partition function Z, we expand the link variable as

$$U_\mu(x) = \exp\{igA_\mu(x)\} = \exp\{igA_\mu^a(x)T_a\} \qquad \text{(B1)}$$

and perform a Fourier transformation

$$A_\mu^a(x) = \frac{1}{\sqrt{N_s^3 N_t}} \sum_k e^{ik(x+\hat{\mu}/2)} A_\mu^a(k), \qquad \text{(B2)}$$

where

$$k_\mu = \frac{2\pi j_\mu}{N_s}, \quad j_\mu = 0, \pm 1, \ldots, N_s/2 \quad \text{for} \quad \mu = 1,2,3,$$

(B3)

$$k_\mu = \frac{2\pi j_\mu}{N_t}, \quad j_\mu = 0, \pm 1, \ldots, N_t/2 \quad \text{for} \quad \mu = 4.$$

(B4)

Fixing the gauge to the lattice Lorentz gauge by adding the gauge fixing term,

$$S_{\rm gf} = -\sum_x {\rm Tr}\left(\sum_\mu \nabla_\mu A_\mu(x)\right)^2,$$

(B5)

the free part of the gauge action [Eq. (2)] is given by

$$S_g^{(0)} + S_{\rm gf}^{(0)} = -\frac{1}{4} \sum_{k,\mu,\nu,a} [q_{\mu\nu}(k)\hat{F}_{\mu\nu}^a(k)\hat{F}_{\mu\nu}^a(-k)$$

$$+ 2\hat{k}_\mu \hat{k}_\nu A_\mu^a(k) A_\nu^a(-k)],$$

(B6)

where $\hat{k}_\mu = 2\sin(k_\mu/2)$, $\hat{F}_{\mu\nu}^a(k) = i[\hat{k}_\mu A_\nu^a(k) - \hat{k}_\nu A_\mu^a(k)]$, and

$$q_{\mu\nu} = 1 - c_1(\hat{k}_\mu^2 + \hat{k}_\nu^2), \quad \text{for} \quad \mu \neq \nu,$$

(B7)

$$q_{\mu\nu} = 0, \quad \text{for} \quad \mu = \nu.$$

(B8)

The free part of the ghost term corresponding to the gauge fixing [Eq. (B5)] is given by

$$S_{\rm gh}^{(0)} = \sum_{k,\mu,a} \hat{k}_\mu \hat{k}_\mu \bar{\eta}^a(-k)\eta^a(k),$$

(B9)

where η and $\bar{\eta}$ are the ghost fields.

The partition function for the gauge part can be calculated as

$$Z_g = \left[\prod_k \det D_{\mu\nu}^{1/2}(k) D_{\rm gh}^{-1}(k) \times (\text{const})\right]^8,$$

(B10)

with

$$D_{\mu\nu}^{-1}(k) = \hat{k}_\mu \hat{k}_\nu + \sum_\rho (\hat{k}_\rho \delta_{\mu\nu} - \hat{k}_\mu \delta_{\rho\nu}) q_{\mu\rho} \hat{k}_\rho,$$

(B11)

$$D_{\rm gh}^{-1}(k) = \sum_\mu \hat{k}_\mu^2.$$

(B12)

Consequently, we obtain the gauge part of the unnormalized free energy density

$$f^{(g)}a^4 = -\frac{1}{N_s^3 N_t} \ln Z_g$$

$$= \frac{8}{N_s^3 N_t} \sum_k{}' \left[\frac{1}{2}\ln(\det D_{\mu\nu}^{-1}(k)) - \ln D_{\rm gh}^{-1}(k)\right] + \text{const},$$

(B13)

where Σ' means a sum except for the zero mode.

The free part of the quark action [Eq. (3)] is given by

$$S_q = -N_f \sum_{a=1}^3 \sum_k \bar{q}^a(k) D_q q^a(k),$$

(B14)

$$D_q(k) = 2K \sum_{\mu=1}^4 \cos(k_\mu) - 1 - 2iK \sum_{\mu=1}^4 \gamma_\mu \sin(k_\mu),$$

(B15)

where

$$k_\mu = \frac{2\pi j_\mu}{N_s}, \quad j_\mu = 0, \pm 1, \ldots, N_s/2 \quad \text{for} \quad \mu = 1,2,3,$$

(B16)

$$k_\mu = \frac{2\pi(j_\mu + 1/2)}{N_t}, \quad j_\mu = 0, \pm 1, \ldots, N_t/2 \quad \text{for} \quad \mu = 4.$$

(B17)

The partition function for the quark part is obtained as

$$Z_q = \left(\prod_k \det D_q(k)\right)^{3N_f}.$$

(B18)

$$\det D_q(k) = \left[\left\{1 - 8K + 4K \sum_{\mu=1}^4 \sin^2(k_\mu/2)\right\}^2 + 4K^2 \sum_{\mu=1}^4 \sin^2(k_\mu)\right]^2.$$

(B19)

We then obtain the quark part of the unnormalized free energy density [31]:

$$f^{(q)}a^4 = -\frac{1}{N_s^3 N_t} \ln Z_q = -\frac{3N_f}{N_s^3 N_t} \sum_k \ln(\det D_q(k)).$$

(B20)

Numerical calculations of the normalized energy density and pressure are performed using the equations

$$pa^4 = -(f^{(g)} - f_{T=0}^{(g)})a^4 - (f^{(q)} - f_{T=0}^{(q)})a^4,$$

(B21)

$$\epsilon a^4 = 3pa^4,$$

(B22)

where $f_{T=0}^{(g)}$ and $f_{T=0}^{(q)}$ are the free energy at zero temperature calculated on an N_s^4 lattice. At the right edge of the Figs. 15, 17, 21, and 23, we show the results for the cases of $16^3 \times 4$ and $16^3 \times 6$ lattices, in the massless quark limit $K = 1/8$.

[1] For a recent review, see S. Ejiri, Nucl. Phys. B (Proc. Suppl.) **94**, 19 (2001).

[2] G. Boyd *et al.*, Phys. Rev. Lett. **75**, 4169 (1995); Nucl. Phys. **B469**, 419 (1996).

[3] CP-PACS Collaboration, M. Okamoto *et al.*, Phys. Rev. D **60**, 094510 (1999).

[4] B. Beinlich *et al.*, Eur. Phys. J. C **6**, 133 (1999).

[5] T. Klassen, Nucl. Phys. **B533**, 557 (1998).

[6] S. Ejiri, Y. Iwasaki, and K. Kanaya, Phys. Rev. D **58**, 094505 (1998).

[7] J. Engels, F. Karsch, and T. Scheideler, Nucl. Phys. **B564**, 303 (2000).

[8] C. Bernard *et al.*, Phys. Rev. D **55**, 6861 (1997).

[9] J. Engels *et al.*, Phys. Lett. B **396**, 210 (1997).

[10] F. Karsch, E. Laermann, and A. Peikert, Phys. Lett. B **478**, 447 (2000).

[11] F. Karsch, Phys. Rev. D **49**, 3791 (1994); A. Berera, *ibid.* **50**, 6949 (1994); F. Karsch and E. Laermann, *ibid.* **50**, 6954 (1994).

[12] S. Aoki *et al.*, Phys. Rev. D **57**, 3910 (1998).

[13] G. Boyd *et al.*, talk given at 10th International Conference on Problems of Quantum Field Theory, Alushta, Ukraine, 1996, hep-lat/9607046; E. Laermann, Nucl. Phys. B (Proc. Suppl.) **63**, 114 (1998).

[14] C. Bernard *et al.*, Phys. Rev. D **61**, 054503 (2000).

[15] M. Fukugita, A. Ukawa, and S. Ohta, Phys. Rev. Lett. **60**, 178 (1988).

[16] C. Bernard *et al.*, Phys. Rev. D **46**, 4741 (1992); C. Bernard *et al.*, *ibid.* **49**, 3574 (1994); T. Bulm *et al.*, *ibid.* **50**, 3377 (1994).

[17] Y. Iwasaki *et al.*, Phys. Rev. D **54**, 7010 (1996).

[18] S. Aoki, Phys. Rev. D **30**, 2653 (1984); Phys. Rev. Lett. **57**, 3136 (1986); Nucl. Phys. **B314**, 79 (1989).

[19] S. Aoki, A. Ukawa, and T. Umemura, Phys. Rev. Lett. **76**, 873 (1996).

[20] S. Aoki, T. Kaneda, A. Ukawa, and T. Umemura, Nucl. Phys. B (Proc. Suppl.) **53**, 438 (1997).

[21] S. Aoki, Y. Iwasaki, K. Kanaya, S. Kaya, A. Ukawa, and T. Yoshié, Nucl. Phys. B (Proc. Suppl.) **63**, 397 (1998).

[22] Y. Iwasaki, K. Kanaya, S. Kaya, and T. Yoshié, Phys. Rev. Lett. **78**, 179 (1997).

[23] Y. Iwasaki, Nucl. Phys. **B258**, 141 (1985); University of Tsukuba Report No. UTHEP-118 (1983).

[24] B. Sheikholeslami and R. Wohlert, Nucl. Phys. **B259**, 572 (1985).

[25] CP-PACS Collaboration, S. Aoki *et al.*, Phys. Rev. D **60**, 114508 (1999).

[26] CP-PACS Collaboration, A. Ali Khan *et al.*, Phys. Rev. D **63**, 034502 (2001).

[27] J. Engels, J. Fingberg, F. Karsch, D. Miller, and M. Weber, Phys. Lett. B **252**, 625 (1990).

[28] CP-PACS Collaboration, A. Ali Khan *et al.*, Phys. Rev. Lett. **85**, 4674 (2000); R. Burkhalter, Nucl. Phys. B (Proc. Suppl.) **73**, 3 (1999).

[29] S. Aoki, R. Frezzotti, and P. Weisz, Nucl. Phys. **B540**, 501 (1999).

[30] CP-PACS Collaboration, A. Ali Khan *et al.*, Nucl. Phys. B (Proc. Suppl.) **83-84**, 360 (2000).

[31] J. Engels, F. Karsch, and H. Satz, Nucl. Phys. **B205**, 239 (1982).

[32] F. Karsch, hep-ph/0103314.